Characterization of Chemical Vapor Deposition Grown Thin film Semiconductor Nanostructure for Optoelectronic Applications

A Synopsis (Approx. 5000 words)

Submitted by

Tamaghna Maitra

Under the supervision of

Prof. Arabinda Nayak

In partial fulfillment for the award of the degree

Of

DOCTOR OF PHILOSOPHY

Department of Physics

Presidency University

Kolkata

Registration No. R– 15RS09110066

Email: *tamaghna.rs@presiuniv.ac.in*

Date of Registration- 12.08.2016

DECLARATION

I hereby declare that the dissertation entitled "***Characterization of Chemical Vapor Deposition Grown Thin film Semiconductor Nanostructure for Optoelectronic Applications"*** to be submitted for the degree of Doctor of Philosophy is my original work and the dissertation has not formed the basis for the award of any degree, diploma, associateship or fellowship of similar other titles. It has not been submitted to any other university or Institution for the award of any degree or diploma.

Place:

Date: (Tamaghna Maitra)

ACKNOWLEDGMENT

The presented work would not have been completed without experimental support and scientic discussion provided by Prof. Satyaban Bhunia, Saha Institute of Nuclear Physics, Kolkata.

1. Introduction

Advanced epitaxial growth of compound semiconductors has contributed enormously to develop new materials and devices in the last few decades. Chemical vapor deposition (CVD), Metal organic chemical vapor deposition (MOCVD) and Molecular beam epitaxy (MBE) nowadays play a significant role in developing low-dimensional nanostructures like quantum wells, QDs, wires, superlattices using conventional III-V compound semiconductor materials like AlGaAs, InGaAs, GaAsP, etc. The low-dimensional nanostructures grown by MBE or MOCVD further find extensive applicability in optoelectronic devices viz., laser structures [1-3], high-efficiency photovoltaic devices [4] and photodetectors [5]. Advanced characterization techniques of the grown materials are equally important for successful device fabrication. In recent years, significant progress in x-ray based characterization techniques of epitaxial thin layers has been achieved in with the advancement of epitaxial growth processes. These x-ray based non-destructive techniques are advantageous for probing the structural and interfacial investigation of such materials at the nanoscale. On the other hand, low-temperature photoluminescence (PL) spectroscopy demonstrates relevant information about various radiative optical transitions including defects present in the synthesized materials. PL is also one of the non-destructive and sensitive methods to exhibit the microscopic structural disorder at the interface i.e. interfacial roughness which affects the performance of the optoelectronic devices. Therefore, in addition to a thorough understanding of these precise epitaxial growth systems, a detailed x-ray and optical characterization of epitaxial thin films is also essential to further tune and optimize the optoelectronic device performance.

In this study, we have planned x-ray based characterization techniques to simulate MOCVD grown $Al_xGa_{1-x}As/Al_yGa_{1-y}As$ spontaneous superlattice structure as well as quaternary AlGaInP thin film. We have also used both the x-ray and PL based analysis for structural and optical studies for the CVD grown vertically aligned ZnO nanowires. For superlattice structure of $Al_xGa_{1-x}As/Al_yGa_{1-y}As$, a combination of x-ray analysis (high angle rocking curve and low angle reflectivity) in conjunction with elaborate simulation based on kinematic diffraction and distorted wave Born approximation (DWBA) of the measured x-ray data has been performed to investigate the compositional variation at the nanoscale and to get an overview of cross-incorporation of atoms at the interfaces. In the case of the quaternary AlGaInP thin film, the structural and optical properties are analyzed with the help of a high-resolution x-ray rocking curve and photoluminescence experiment. The depth profile of the film structure was obtained from the x-ray rocking curve simulation. The low-temperature photoluminescence study also

gives insight into the defect levels in the material. For the optoelectronic device applications, a symmetric coplanar metal-semiconductor-metal (MSM) structure has been successfully fabricated on epitaxially grown quaternary thin film for photodetection in the visible part of the electromagnetic spectrum. In the case of vertically aligned ZnO nanowires, a detailed x-ray characterization technique for the two different geometries, viz., θ-2θ scan and Φ-scan has been carried out to comprehend the ultraviolet lasing from the optically pumped nanowire ensembles. The PL analysis of the optically pumped nanowires at a low temperature of 3.4 K and different elevated temperatures have been performed to understand the lasing behavior.

2. Literature Review

2.1 Spontaneous ordering in $Al_xGa_{1-x}As$ epilayer

Monolayer scale spontaneous superlattice formation have been observed by several researchers in epitaxial films of III-V compound semiconductors like ternary AlGaAs [6], GaInP [7-9], AlInAs [8], AlInP [10], GaAsSb [11], etc. grown either by Metal Organic Chemical Vapor Deposition (MOCVD) or Molecular Beam Epitaxy (MBE) technique. A Cu-Pt type long-range monolayer ordering is observed in $Ga_{0.49}In_{0.51}P$ epilayers independently by both R. T. Lee et al. and M. Kondow et al. [12, 13]. Such kind of atomic-scale ordering is a common and naturally occurring phenomenon in the III-V ternary and quaternary alloy system and well established thermodynamically by considering enthalpy of mixing as explained by M. Ichimura et al. [14]. Owing to the miscibility of the components over an entire range of composition and large excess enthalpy, long-range spontaneous ordering in $Al_xGa_{1-x}As$ system was considered to be quite unusual [15, 16]. The MOCVD grown atomic-scale ordering in $Al_xGa_{1-x}As$ layer on (110) or (100) GaAs substrates with different Al compositions was first noticed in 1985, where clear segregation of GaAs and AlAs atomic monolayer was observed by T. S. Kuan et al. at different growth temperatures [6]. W. I. Wang et al. explained this kind of phenomenon by charge transfer dipole stabilization model [17]. Long-range spontaneous ordering in AlxGa1-xAs epilayer over multiple atomic layers grown by MBE was reported earlier by M. E. Hoenk et al. [18]. Very recently, we have reported for the first time a long-range ordering in MOCVD grown $Al_xGa_{1-x}As$ layers on (001) GaAs [19] with about twenty monolayer length scale. X-ray reflectivity (XRR) technique is used here to find out the electron density profile (EDP) as a function of depth in the ordered structure under the framework of distorted wave Born approximation (DWBA) due to S. K. Sinha et al. [20] and this EDP further provides information regarding composition as well as interdiffusion [21]. The DWBA technique includes higher-order corrections owing to multiple reflections from each layer of the thin film

as compared to the first-order Born approximation [20]. It is already a very well established and proven tool in extracting the thickness and compositional fluctuation at the nanoscale. The broad range of applicability of this procedure ranges from Cadmium Arachidate Langmuir-Blodgett (LB) film [21] to artificial Si-Ge superlattice structures [22].

2.2 Fast-response Symmetric Coplanar Ni/AlGaInP/Ni Visible Photodetector

The quaternary AlGaInP has been primarily used as a top window layer in a tandem solar cell due to its wide bandgap due to Van Riesen et al. [23], high brightness light emitting diodes (LED) by Vanderwater et al. and Streubel et al. [24, 25] and high electron mobility transistors due to Wang et al. [26]. Lothian et al. [27] have shown that the quaternary AlGaInP had higher etching selectivity over other III-V semiconductors. Watanabe et al. [28] had found that it had a higher conduction band offset compared to other semiconductors. Lee et al. [29] incorporated a thin capping layer of this material lattice-matched to GaAs to enhance the performance of a metal-semiconductor-metal photodetector (MSM) based on GaAs, operating in the near-infrared region.

2.2 Ultraviolet lasing from vertically aligned ZnO nanowires

Ultraviolet (UV) lasing from monocrystalline semiconductor nanowires (NWs) such as AlGaN due to Zhao et al. [30], single-mode GaN by Behzadirad et al. [31] and ZnO by several researchers [32-34] has recently received widespread attention. UV random lasing action has been observed [35-39] in disordered particles and thin films of ZnO by several researchers. Klingshirn et al. [40] have discussed that wide band-gap semiconductor materials usually require a high carrier concentration to reach an optical gain large enough for the onset of lasing in an electron-hole plasma (EHP) process. Alternatively, Wegscheider et al. [41] showed that the excitonic recombination in semiconductors was a more efficient radiative process and could alleviate the high threshold of stimulated emission as required in an EHP process. Low threshold lasing from semiconductor NWs has been previously reported in GaAs by Alanis et al. [42] and Ge systems by Bao et al. [43]. Stimulated emission and optical gain have also been demonstrated in electrically pumped Sb doped p-ZnO and undoped n-ZnO NWs by Chu et al. [32]. Huang et al. [44] have demonstrated lasing action in ZnO NWs arrays at room temperature.

3. Theory

3.1 X-ray reflectivity (XRR) and rocking curve (XRC) simulations

3.1.1 Modeling of x-ray reflectivity profiles for superlattice structure

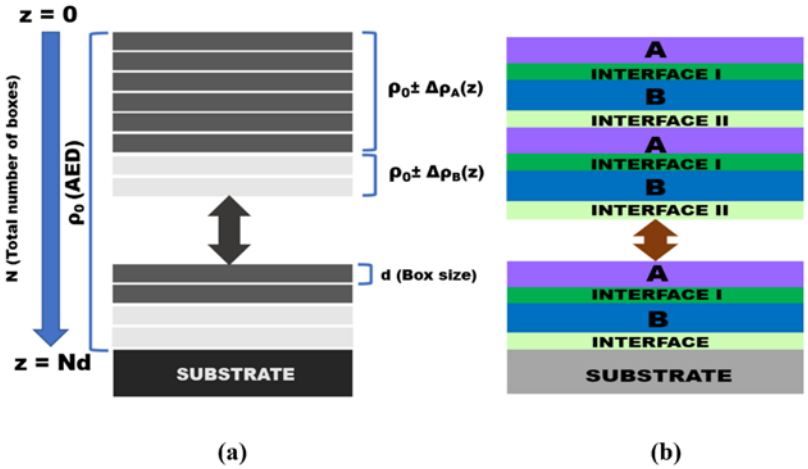

Fig. 1. (a) Model structure to simulate specular x-ray reflectivity data using DWBA formalism **(b)** Schematic model structure to simulate x-ray rocking curve using kinematical theory of X-ray diffraction.

Grazing angle XRR owing to small penetration of x-rays probes surface atoms to a large extent. Here we have utilized the DWBA technique [20] to analyze the XRR data of MOCVD grown $Al_xGa_{1-x}As/Al_yGa_{1-y}As$ spontaneous superlattice structure. In this process, the total multilayer stack is divided into *N* number of finite thin boxes of equal thickness *d* as shown in Fig. 1(a).

The electron density (ED) corresponding to each layer is represented as $\rho_0+\Delta\rho(z)$ where ρ_0 is the average electron density (AED) of the multi-stack film and $\Delta\rho(z)$ is the fluctuation in ED over the average value as a function of depth *z*, where the top surface of the film is considered to be at *z*=0. The ED of the i-th box from the top surface is expressed as $\rho_0+\Delta\rho_i(z)$ for DWBA analysis. Fourier transformation of $\Delta\rho(z)$ leads us to write

$$\Delta\rho(q_z) = \int_{-\infty}^{\infty} \Delta\rho(z) \exp(iq_z z)\, dz \qquad (1)$$

This integral is recast in the following form,

$$\Delta\rho(q_z) = \frac{i}{q_z}[(\sum_{j=1}^{N}(\Delta\rho_j - \Delta\rho_{j-1})\exp\{iq_z(j-1)d\}) + \Delta\rho_1 - \Delta\rho_N \exp(iq_z Nd)] \qquad (2)$$

Where q_z is the *z* component of momentum transfer in the multilayer film and is given as $2(k^2-k_c^2)^{1/2}$ where $k = q_z/2 = (2\pi \sin\theta)/\lambda$ is the wave vector associated with the grazing angle θ and k_c is the value of it corresponding to the critical angle θ_c. In DWBA the specular reflectivity $R(q_z)$ of the multilayer system turns out to be [21,22]:

$$R(q_z) = |ir_0(q_z) + \frac{4\pi r_e}{q_z}[a^2 \Delta\rho(q_z) + b^2 \Delta\rho^*(q_z)]|^2 \quad (3)$$

Where $r_0\ (q_z)$ is the specular reflectance coefficient of the multilayer film with AED ρ_0, $a(q_z)$ and $b(q_z)$ are the coefficients for the transmitted and reflected amplitudes in the average film. A simplex based nonlinear least square fitting program is employed to fit the reflectivity data on the basis of DWBA formalism of the model of Fig. 1(a). From this fitted EDP, the aluminum *(x)* and gallium *(1-x)* composition profile are calculated using Vegard's law as follows,

$$x = \frac{EDP_{GaAs} - EDP_{FILM}}{EDP_{GaAs} - EDP_{AlAs}} \quad (4)$$

3.1.2 Modeling of rocking curve profiles for superlattice structure

For the analysis of x-ray rocking curves, we have considered a model [45-47] based on kinematical diffraction theory, the schematics of which is presented in Fig 1(b). For each superlattice period consisting of two layers and two interfaces in between them, we calculate its structure factor F_0. The whole superlattice structure factor F_{SL} is the sum of the 'F_0's along with their phase factors of all the bilayers. Thus, the structure factor of a one-dimensional superlattice can be expressed as,

$$F_{SL}(q) = \sum_{p=0}^{N-1} F_0 e^{iqN\Lambda} \quad (5)$$

where q is the scattering vector along the (001) direction, Λ is the superlattice periodicity and N is the total number of bilayer periods and F_0 is given as [45]

$$F_0 = f_A \sum_{n=0}^{N_A-1} e^{iq2nd_A} + f_{AB} e^{iq2N_A d_A} \sum_{n=0}^{N_{AB}-1} e^{iq2nd_{AB}} +$$

$$f_B e^{iq2(d_A N_A + d_{AB} N_{AB})} \sum_{n=0}^{N_B-1} e^{iq2nd_B} + f_{BA} e^{iq2(d_A N_A + d_{AB} N_{AB} + d_B N_B)} \sum_{n=0}^{N_{BA}-1} e^{iq2nd_{BA}} \quad (6)$$

The subscripts *A, B, AB* and *BA* with different factors '*d'* stand for the different layers as shown in the schematic representation of the superlattice structure. The structure factor corresponding to the substrate Bragg reflection is given by [48],

$$F_{sub}(q) = f_s \frac{1-\exp(iq2Pd_s)}{1-\exp(iq2d_s)} \quad (7)$$

where f_s and d_s are the atomic scattering factors and lattice spacing between atomic planes of group-III and V elements for the substrate material, respectively and 'P' is the total number of atomic planes in the substrate material. The total diffracted intensity will be

$$I(q) = |F_{SL} + F_{sub}|^2 \quad (8)$$

3.1.3 Modeling of rocking curve profiles for quaternary thin film

In case of the quaternary thin film, eq. 8 has been modified by substituting the contribution from the superlattice layer with that of the thin film layer to further simulate the x-ray diffraction pattern

$$I(q) = |\sum_{n=0}^{N}(A_n exp[i\sum_{j=0}^{n} a_j q_z]) + F_{sub}|^2 \quad (9)$$

3.2 Electrical simulations

The current (I) flowing through MSM structure could be extracted from the total voltage drop ($V=V_1+V_2$) across the metal-semiconductor junctions as [49],

$$I = \frac{2\, I_{01}(V_1) I_{02}(V_2)\, sinh\left(\frac{qV}{2\eta k_B T}\right)}{I_{01}(V_1) exp\left(-\frac{qV}{2\eta k_B T}\right) + I_{02}(V_2) exp\left(\frac{qV}{2\eta k_B T}\right)} \quad (10)$$

which has been employed to simulate the dark I-V characteristics of the MSM structure and to extract the ideality factor and the barrier heights.

4. Experimental work

The reported epilayer of $Al_xGa_{1-x}As$ on semi-insulating GaAs (100) substrate was grown by the MOCVD process. Trimethylgallium (TMG) and trimethylaluminum (TMA) were used as group III sources while Arsine (AsH3) was used as a group V source. The growth temperature and time were optimized to 650^o C and 5 min, respectively giving a nominal epilayer thickness of about 2000 Å.

The $(Al_xGa_{1-x})_y In_{1-y}P$ thin film was grown on (100) SI-GaAs substrates by MOCVD technique using Trimethyl aluminum (TMA), Trimethylgallium (TMG), and Trimethylindium (TMI) as group III precursors whereas Phosphine (PH_3) as group V source. A thin GaAs buffer layer of 400 Å was grown on the substrate prior to the growth of the quaternary thin film. The reactor pressure, growth temperature, growth rate, and V/III ratio were maintained at 100 mbar, 650° C, ~2 µm/hr, and 176, respectively. Nickel (Ni) metallic foils (Loba Chemie, 99.9 % pure)

were evaporated on the top of the quaternary thin film by thermal evaporation using proper masking arrangements.

Vertically oriented ZnO NWs in the form of thin films were grown on c-plane (0001) sapphire substrate by a catalyst-free chemical vapor deposition (CVD) method with N2 and O2 being the carrier and reactant gas, respectively. The 99.999 % pure Zinc acetate dehydrate (Zn $(CH_3COO_2)_2$. 2 H_2O) in powder form was procured from Sigma-Aldrich and was used without any further purification. For each growth, typically about 500 mg of zinc acetate powder was taken as a source, which was placed at a quartz boat of the two-zone CVD reactor. The source temperature was fixed at 250^o C which is above its sublimation temperature of ~235^o C. The growth temperature was fixed at 300^o C. The duration of a single growth was about 5 minutes. The flow ratio of N_2 and O_2 as the carrier and reactant gases were kept fixed at 1.5.

All x-ray measurements were carried out at Indian Beamline, BL-18B at Photon Factory, Japan. The x-ray wavelength was taken to be 1.089 Å. The spontaneous superlattice structures were analyzed by high-resolution cross-sectional TEM images taken in a Tecnai G2 F30 S-TWIN instrument operating at 300 kV. The room temperature I-V characteristics were performed using a Keithley 4200 semiconductor characterization system. Spectral response of the MSM photodetector from 300-1000 nm was evaluated using an experimental arrangement consists of a 450W Xenon lamp and a monochromator (Model-Gemini 180, Horiba Jovin Yvon).

5. The aim of the thesis and its achievements in that perspective

5.1 Evaluation of spontaneous superlattice ordering in MOCVD grown $Al_xGa_{1-x}As$ epilayer on GaAs (100) using X-ray reflectivity and rocking curve analysis

In this work, we have presented a comprehensive high-resolution x-ray reflectivity and rocking curve analysis for MOCVD grown $Al_xGa_{1-x}As/Al_yGa_{1-y}As$ spontaneous superlattice structure. A combination of x-ray analysis such as high angle rocking curve and low angle reflectivity of this type of superlattice structures could be useful to extract the compositional information and to get an overview of cross-incorporation of atoms at the interfaces. The DWBA method has been implemented to simulate the measured XRR data to obtain the composition profile, interfacial diffusion, and composition. The compositional information obtained from DWBA simulation was then applied to fit the x-ray rocking curves (XRC) of the ordered structure using the kinematical model of x-ray diffraction and bring out the stoichiometric information of the superlattice structure.

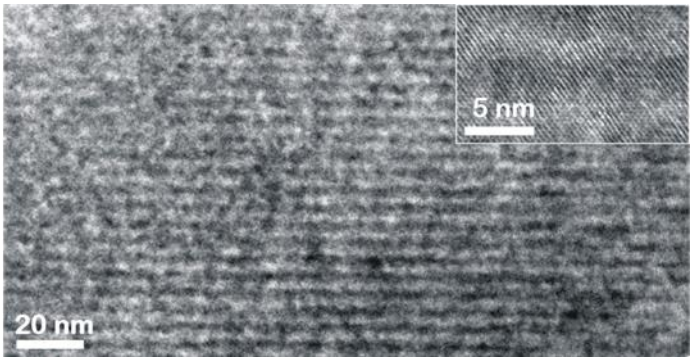

Fig. 2. Cross sectional transmission electron microscopic image of the spontaneous superlattice structure. Inset shows the high-resolution image.

In the case of our spontaneously formed superlattice structure, the total thickness of 2104 Å is taken which corresponds to a total epilayer of 2028 Å plus some part of the substrate layers as the contribution from the substrate to the XRR curve can't be ignored for such epitaxial thin film. The periodicity of the superlattice as determined from the separation of the consecutive peaks in the XRR curve was found to be 52 Å. The cross-sectional TEM image shown in Fig. 2 also gives a value of the period thickness of similar value. For simulation, the number of elemental boxes was taken to be 526 and the size of each box is chosen as 4 Å. The average electron density (ρ_0) for this sample was chosen to be 1.2644 $Å^{-3}$ which corresponds to grown epilayer having an average aluminum composition of 0.17. The experimental reflectivity curve is shown in Fig. 3(a) exhibits a series of nearly equidistant sharp peaks giving a clear indication of highly ordered superlattice structure in the epilayer.

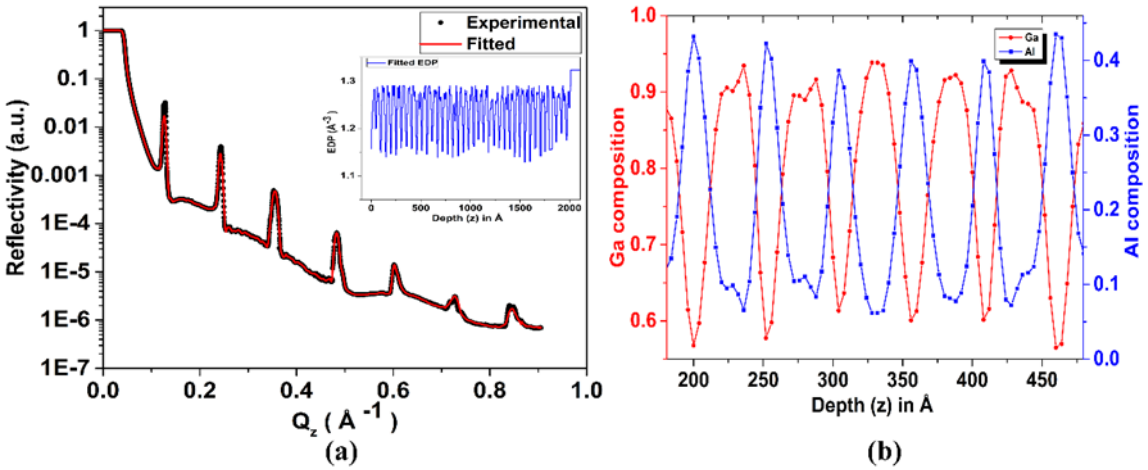

Fig. 3. (a) Experimental and DWBA fitted XRR curve of spontaneous superlattice structure. Inset shows the fitted electron density profile of the superlattice as obtained from the simulation of the measured XRR data **(b)** Compositional modulation of aluminum (gallium) throughout a certain depth of the superlattice structure.

The simulated curve superimposed on the experimental data in Fig. 3(a) shows excellent agreement. The EDP as a function of depth generated from the fitting procedure is shown in the inset of Fig. 3(a). The aluminum compositions x and y of the superlattice structure, obtained using Eq. 4 is shown in Fig. 3(b). For sake of clarity, the plot is shown only up to a depth of 475 Å. The Al (Ga) composition modulation was found to vary between 0.1 and 0.4, thus giving a superlattice bilayer structure of $Al_{0.1}Ga_{0.9}As/Al_{0.4}Ga_{0.6}As$. The obtained compositional information from the reflectivity fitting was then applied for fitting the rocking curves.

The rocking curve pattern of the spontaneous superlattice structure shows symmetrical nature around the zeroth order (central) satellite peak which coincides with the weak substrate Bragg peak in case of (002) (Fig 4 (a)) and around the main Bragg peak in the case of (004) (Fig 4 (b)). Both the rocking curves were consisted of sharp and strong equidistant peaks on both sides of the zeroth-order peak. This fact implies that there was no effective strain developed in the sample and the presence of the higher-order satellites was due to modulation in composition alone. Excellent agreement was found between the experimental and simulated curves. From the simulation, we have again found the superlattice periodicity of about 52 Å which is repeated 39 times to construct the multilayer stack in the $Al_xGa_{1-x}As/Al_yGa_{1-y}As$ epitaxial layer.

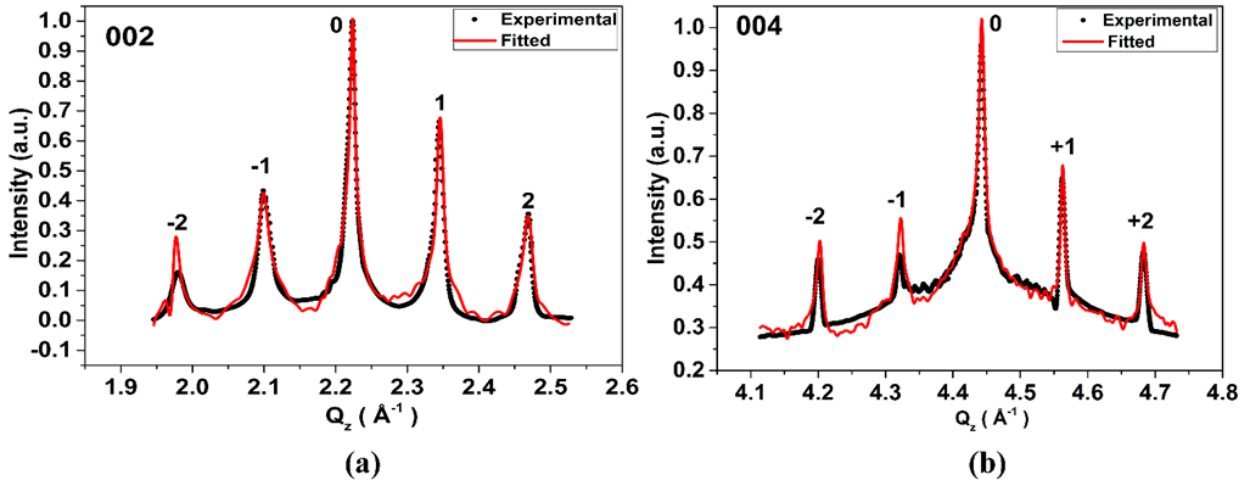

Fig. 4. (a) (002) and **(b)** (004) XRC of spontaneous superlattice structure fitted using kinematical theory of X-ray diffraction.

The thicknesses of the two layers A and B were 8 Å and 24 Å which are about 3 and 8 monolayers respectively. Information about the two interfaces was also obtained from the simulation. The interface thickness between layers A and B and that between B and A were 12 Å and 8 Å, respectively. The Al compositions of layers A and B are found out to be 0.14 and 0.36 respectively. The Al compositions at the interface i.e. compositions of layers AB and BA are determined to be of 0.18 and 0.26 respectively. These parameters agree quite well with

those extracted from the previous XRR analysis as well as cross-sectional HRTEM image (thickness) of the grown superlattice structure.

5.2 Fast-response Symmetric Coplanar Ni/AlGaInP/Ni Visible Photodetector

A symmetric coplanar metal-semiconductor-metal structure has been successfully fabricated on MOCVD grown quaternary thin film $(Al_xGa_{1-x})_y In_{1-y}P$ / (100) semi-insulating GaAs (SI-GaAs) substrate for photodetection in the visible part of the electromagnetic spectrum. Before the fabrication of the device, the structural depth profile of the material was extracted using the kinematical theory of X-ray diffraction. X-ray diffraction results shown in Fig. 5 (a), carried out on the film exhibit two sharp and prominent peaks, clearly indicating good crystallinity of the material. The strong peak at $2\theta = 22.65^o$ corresponds to the reflection from (004) plane of GaAs buffer/substrate, while the one at the right side of this peak at $2\theta = 22.95^o$ corresponds to $(Al_yGa_{1-y})_z In_{1-z} P$ film. The simulated results of the depth profile of the film structure are shown in the inset of Fig. 5 (a). The lattice constants of the epilayers are found to be 5.6532

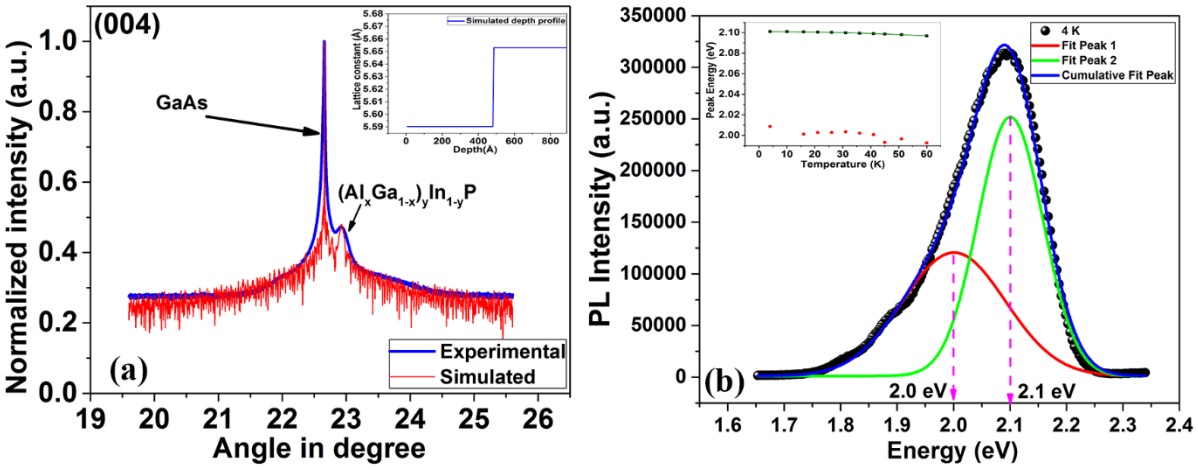

Fig. 5. (a) Experimental (solid blue line) and simulated (solid red line) X-ray rocking curve of the quaternary sample (Inset shows the simulated depth profile as obtained from the kinematical theory of X-ray diffraction) (b) The PL spectra at 4K. Inset shows the variation of the two peak energies with temperature.

Å for GaAs and 5.5901 Å for $(Al_xGa_{1-x})_y In_{1-y} P$. Using Vegard's law, the composition 'y' of the alloy is estimated as ~ 0.66 which suggests that the grown quaternary film is not exactly lattice-matched to the GaAs substrate.

The Low temperature (4 K) PL spectra of the films shown in Fig. 5 (b) exhibit a broad peak suggesting the presence of near band edge defect-related states. The single broad peak is deconvoluted into a stronger higher energy component due to bandgap related excitonic transition at 2.1 eV and a broad overlapping peak at a lower energy of 2.001 eV due to defect-

related states. These two peaks at their respective energy positions have been fitted well with two Gaussian lineshape functions as evident from Fig. 5 (b). The origin of the two peaks has been further confirmed from the plot of peak position as a function of temperature as shown in the inset of Fig. 5 (b). The values of the three Varshni parameters, E_{g0}, α, and β are found to be 2.101 eV, 5.23.x10^{-4} eV/K and 383.205 K, respectively. These values are further used to obtain the 'x' composition value of 0.67.

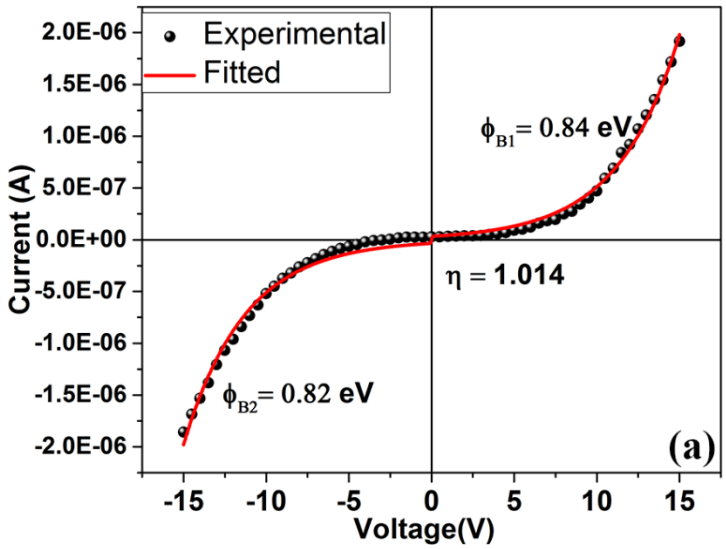

Fig. 6. Experimental (black solid spheres) and simulated (red line) dark I-V curve using a simple two back-to-back connected diode model.

Fig.6 shows the experimental (solid black ball) and fitted (solid red line) dark I-V characteristics of the device. Eq. 10 has been used to fit and extract the barrier heights φ_{B1} and φ_{B2} and ideality factor η of the MSM structure. The effective barrier height at the two symmetric nickel contact comes out to be $\phi_{B_1}^{E}$ =0.84 eV and $\phi_{B_2}^{E}$= 0.82 eV. The fitted ideality factor η = 1.014 deviated slightly from that of the ideal Schottky barrier (η = 1) [50, 51] which also proves the formation of good quality Schottky contacts.

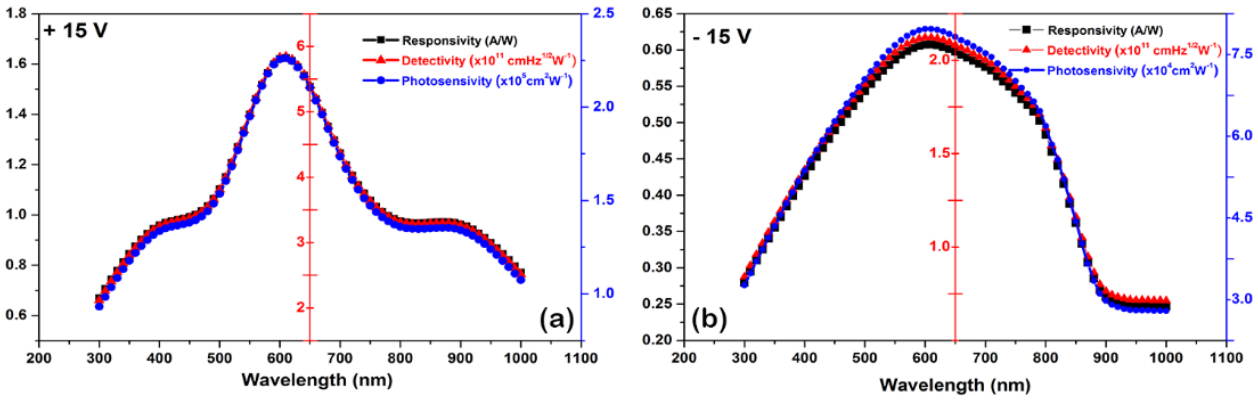

Fig. 7. Plot of three different figure of merit as a function of wavelength for the MSM PD at two different applied bias of **(a)** +15 V and **(b)** -15 V respectively.

Fig. 7 (a) and (b) show the variability of *R*, *D*, and *S* as a function of the wavelength of illumination varying from 300 nm to 1000 nm, at a constantly applied voltage bias of +15 V and -15 V, respectively. The device operability could be found between 500 and 800 nm with a peak at 610 nm. The maximum peak responsivity, detectivity, and photosensitivity at a fixed bias of +15 V were estimated to be 1.62 AW^{-1}, 6.34x10^{11} $cmHz^{1/2}W^{-1,}$ and 2.26x10^{5} $cm^{2}W^{-1}$, respectively, and at -15 V these became 0.6 AW^{-1}, 2.37x10^{11} $cmHz^{1/2}W^{-1}$, and 8.72x10^{4} cmW^{-1}, respectively in the presence of illumination wavelength of 610 nm with a constant optical power of 2 $\mu W/cm^2$.

The key parameters viz. response time and time of recovery for an MSM photodetector essentially depend on the lifetime of the trapped photogenerated carriers in the trap states being present in the quaternary thin film. A few cycles vis-a-vis temporal variation of the measured normalized photocurrent is presented in Fig.8 (a) and an enlarged image of only one cycle is shown in Fig. 8 (b). The device photocurrent showed an abrupt rise under illuminated condition

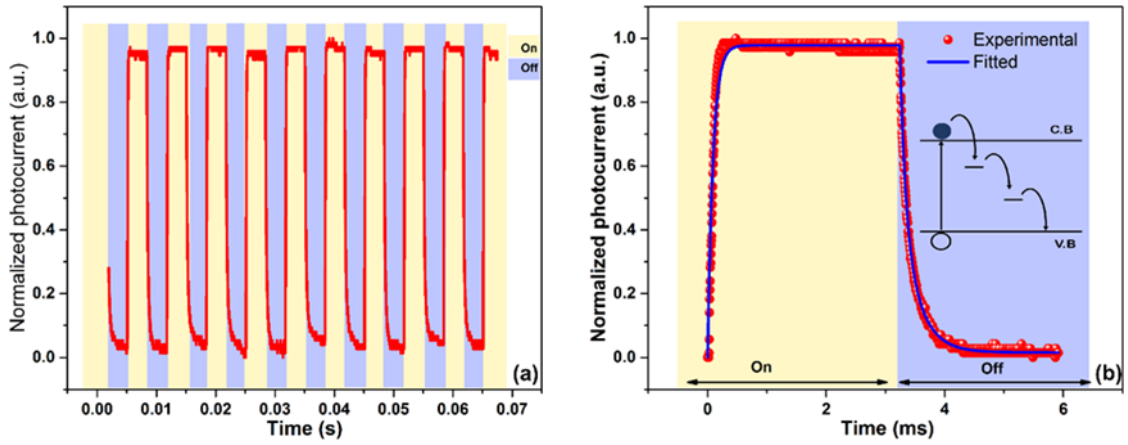

Fig. 8. (a) The time response of the device at a fixed frequency of 150 Hz **(b)** Enlarged view of one cycle with experimental (red solid spheres) and fitted (blue solid line) data. Inset shows the mechanism of the relaxation of the photogenerated carriers.

(Fig. 8 (b)) (ON condition) followed by a comparably slower decay of photocurrent when the light is turned off. The time of rising (τ_r) is evaluated by fitting the experimentally obtained data using the following equation

$$I = I_d + A\left(1 - \exp\left(-\frac{t}{\tau_r}\right)\right) \tag{11}$$

providing the value of τ_r = 91 μs which is quite fast. This fast responsiveness of the device could be correlated to the band to band transition.

The decay curve was fitted with two-channel decay exponentials to extract the time of recovery,

$$I = I_L\left(A\exp\left(-\frac{t}{\tau_{d1}}\right) + B\exp\left(-\frac{t}{\tau_{d2}}\right)\right) \quad (12)$$

The existence of dual decay channels has been clearly manifested in Eq. (12). The time of recoveries τ_{d1} and τ_{d2} are found to be 83 μs and 282 μs, respectively. The temporal response of this photodetector is quite fast in comparison to other similar devices made using various semiconductor materials.

5.3 Temperature and excitation dependent ultraviolet lasing in vertically oriented ZnO nanowires

In this study, vertically oriented ZnO NWs in the form of thin films were grown on c-plane (0001) sapphire substrate by a catalyst-free chemical vapor deposition (CVD) method. Herein we report detailed collective analysis of structural, morphological and optical properties to investigate the lasing phenomena from ZnO NWs at a low excitation density by high-resolution X-ray diffraction, scanning electron microscopy and variable temperature and excitation power-dependent photoluminescence measurements.

The SEM micrograph (**Fig. 9**) prominently shows vertically oriented hexagonal facets of individual NWs indicating good crystalline quality. The average length and diameter of the nanowires were found to be about 0.9 μm and 0.4 μm, respectively. The SEM images were taken at a tilt angle of 40.1°. The energy dispersive x-ray (EDX) measurement is shown at the inset of Fig. 9, which clearly shows peaks due to Zn and O. The average stoichiometry ratio of Zn:O, calculated from the integrated intensities and the sensitivity factors of the corresponding elements (Zn, O), was found to be within the desired range of 1:1 to the accuracy of ± 10 % of the detection limit of the EDX spectrum.

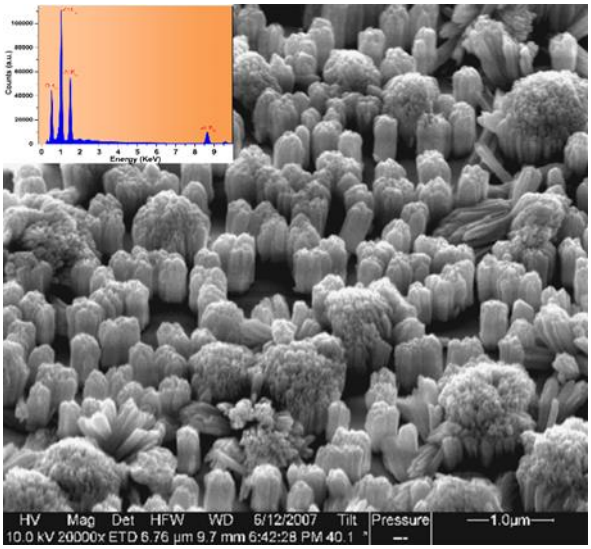

Fig. 9. SEM image of vertically aligned ZnO nanowires bundles grown at 300°C. Inset of Fig. 1 shows the typical EDX spectra of the grown sample.

Fig. 10 shows a typical XRD pattern of the ZnO NWs. Here, we have observed only a sharp and dominant (002) and its harmonic (004) diffraction peaks at 30.37° and 68.52°, respectively. This indicates that for our nanowire bundles, there was a strong preferential orientation along the c-axis, which is also the growth direction of the nanowires. The out of plane lattice constant 'c' comes out to be of 5.2468 Å as evaluated from the (002) peak. The out-of-plane tensile strain was calculated using $\frac{c_{nw}-c_{bulk}}{c_{bulk}} \times 100\% = 0.8\ \%$ where $c_{bulk} = 5.205$ Å [52]. This small amount of strain suggests a very high structural quality of the nanowires which in turn reflects into the enhancement of optical gain to sustain cavity modes. Moreover, the appearance of a very sharp (002) peak with the narrow full width at half maximum (FWHM) of around 0.17° in the θ-2θ scan predicts unambiguously directional growth of single-crystal structure of the nanowire, free from any mosaicity and twin boundaries.

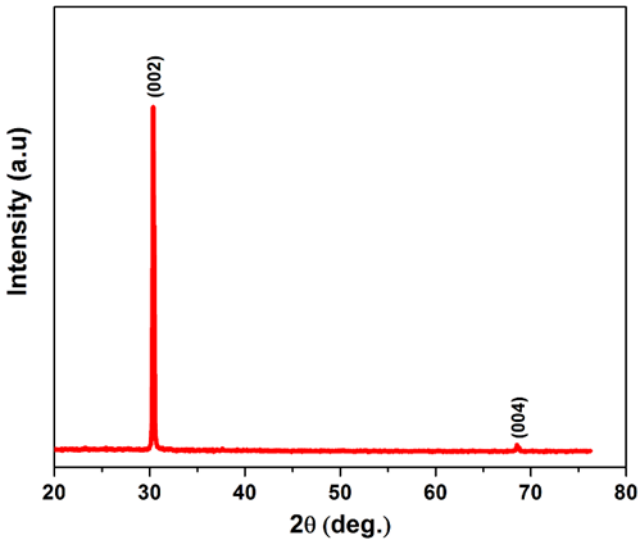

Fig. 10. Powder XRD patterns of vertically oriented ZnO nanowires

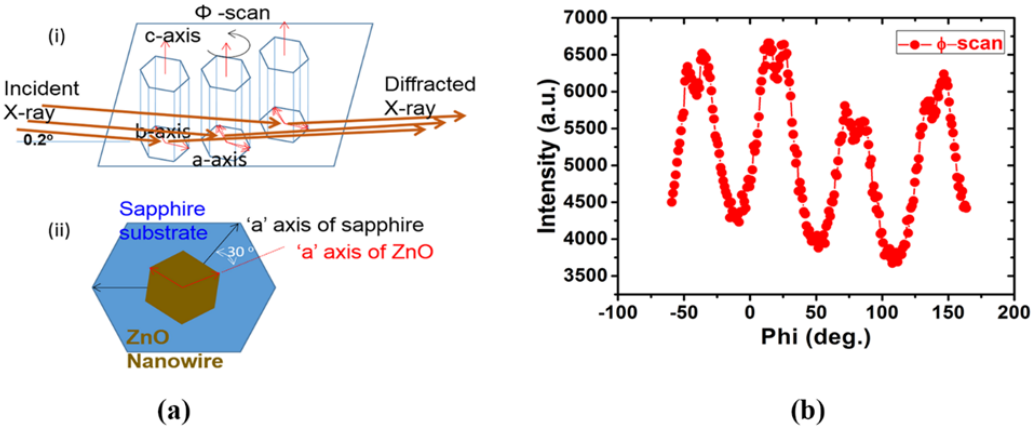

Fig. 11. (a) Schematic representation of (i) grazing incidence X-ray diffraction geometry and relative orientation of 'a' and 'b' axes of ZnO nanowires with respect to each other. (ii) crystallographic orientation of ZnO nanowires on sapphire substrates **(b)** A typical Φ-scan of vertically oriented nanowire bundles of ZnO.

To investigate the relative in-plane lattice alignment 'a' and 'b' of the individual NWs with respect to one another as illustrated in **Fig. 11 (a)**, the detector was first scanned in the horizontal plane to find the first peak at an in-plane angle of 28.6°, which corresponds to the$\{10\bar{1}0\}$ family of planes of the NWs having a d-spacing of 2.81 Å. Keeping the detector fixed at this angle, the sample was then given an in-plane rotation. **Fig. 11 (b)** shows diffraction intensity vs Φ angle in the range of - 60° < Φ < 160° for the NWs. The presence of four peaks at a quite regular interval of 60° signifies not only the 6-fold symmetry of ZnO NWs but also a high degree of coherence in the in-plane orientation of individual NWs. The Φ-scans under grazing incidence is illustrated in Fig.11 (b).

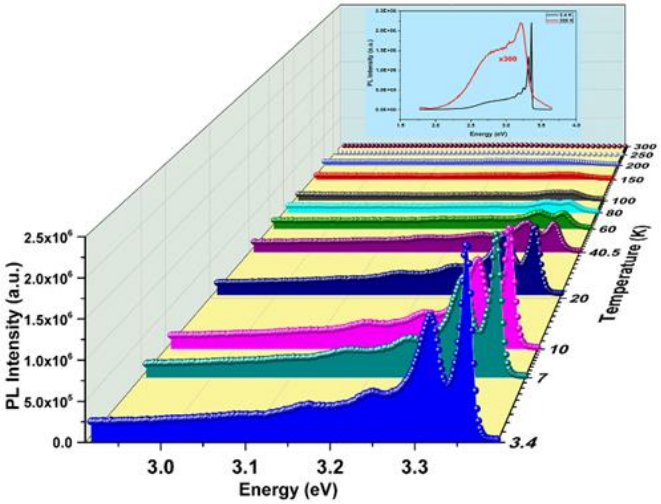

Fig. 12. Waterfall plot of temperature dependent PL spectra at a fixed excitation power of 14.52 mW (Inset shows PL spectra at 3.4 K and at 300 K @14.52 mW of excitation power respectively).

Fig. 12 shows the plot of the temperature-dependent PL intensity of the grown NWs as a function of excitation energy with a fixed excitation power of 14.52 mW. Inset of Fig. 12 shows the PL spectra of the NWs at room temperature and 3.4 K. The room temperature spectra consisted of two peaks. The higher energy peak at 3.213 eV was originated from the radiative recombination of free excitons while the broad peak at lower energy was mostly attributed to the recombination of electrons in singly ionized oxygen vacancies (Vo^{+}) with photo-excited holes in the valence band [53]. The spectra at 3.4 K consisted mainly of band edge related features with a sharp dominant peak at 3.361 eV having a full width at half maximum (FWHM) of 13 meV which is about 14 times less as compared to the room temperature PL spectra with negligible defect-related intensity.

Fig. 13 shows a plot of excitation dependent intensities at 3.4 K (excitonic peaks along with the two sub-bands as a function of excitation power) and room temperature (excitonic peak along with defect peak as a function of excitation power), respectively. A sharp enhancement

in emission intensity of the peak for excitation power > 14.52 mW was observed, which is the main characteristic of lasing from NWs as confirmed from the sigmoidal nature of the log-log plot of intensity vs excitation power (Inset of **Fig. 13**). This is quite different from the excitation dependent intensity observed at room temperature as shown in the inset of **Fig. 13**, where a monotonous increase in intensity with excitation power was observed.

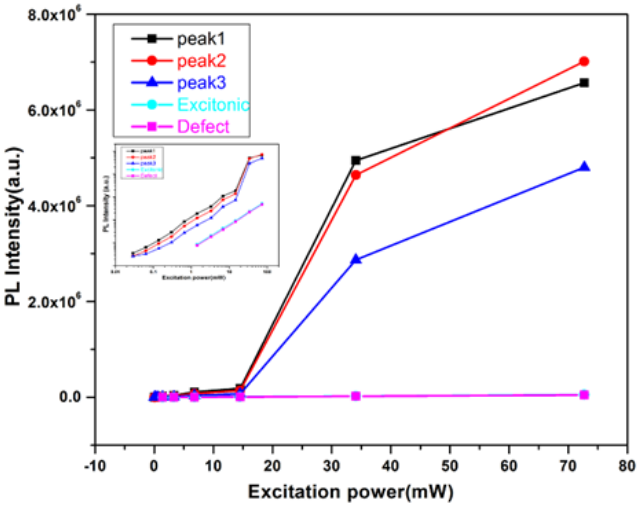

Fig. 13. Plot of intensities of the main peak along with the two sub-band at 3.4 K and the defect at 300 K as a function of excitation power. The lasing characteristics is evident from the sigmoidal nature of the log-log plot of intensities of the three peaks at different optical excitation levels at 3.4 K as shown in the inset.

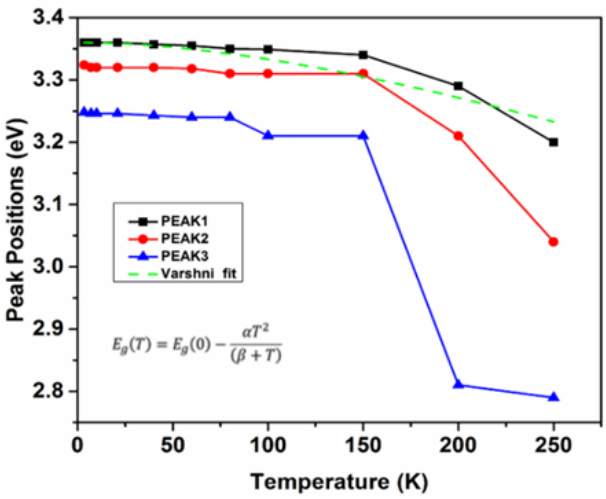

Fig. 14. Plot of the positions of the three peaks at different temperatures. Green dotted line shows the theoretical Varshni plot.

Fig. 14 shows the positions of the main excitonic peak along with the two lower energy peaks. The positions of all the three peaks remained unchanged up to the characteristic temperature of 150 K, beyond which the positions of all the three peaks red-shifted with the increase in temperature. For further understanding, the nature of the shift, a plot of the theoretical shift in

bandgap as a function of temperature was carried out, often described by an empirical relationship, known as the Varshni's equation [54] given as

$$E_g(T) = E_g(0) - \frac{\alpha T^2}{(\beta + T)} \quad (13)$$

where α and β are material dependent parameters. The parameter β is proportional to Debye temperature θ_D. The values for α and β are taken to be 8.2 x 10^{-4} eV/K and 50 K, respectively. The theoretical plot is shown as the green dotted line in **Fig. 14**. Understandably, the characteristic of none of the peaks matches that of the bandgap of ZnO and fundamentally they are different, especially below the characteristic temperature of 150 K. However, above 150 K, the peak positions changed differently with increasing temperature.

References

1. A.V Babichev, L.Y. Karachinskii, I.I. Novikov et al., Vertical-Cavity Surface-Emitting 1.55-μm Lasers Fabricated by Fusion Tech. Phys. Lett, 44: 24. (2018).
2. H. Hatakeyama, T. Anan, T. Akagawa, K. Fukatsu, N. Suzuki, K. Tokutome, and M. Tsuji, Highly Reliable High-Speed 1.1μm-Range VCSELs With InGaAs/GaAsP-MQWs, IEEE J. Quantum Electron. 46(6), 890 (2010).
3. T. Walther, A.B. Krysa, Transmission electron microscopy of AlGaAs/GaAs quantum cascade laser structures, Journal of Microscopy, 268 (3), 298 (2017).
4. K. Toprasertpong, H. Fujii, T. Thomas, M. Fuehrer, D. Alonso-Alvarez, D. J. Farrell, K. Watanabe, Y. Okada, N. J. Ekins-Daukes, M. Sugiyama, and Y. Nakano, Absorption threshold extended to 1.15 eV using InGaAs/GaAsP quantum wells for over-50%-efficient lattice-matched quad-junction solar cells, Prog. Photovoltaics: Res. Appl. 24, 533 (2016).
5. A.Pradhan, S. Mukherjee, T. Maitra, S. Mukherjee, A. Nayak, S. Bhunia, Improved spectral and temporal response of MSM photodetectors fabricated on MOCVD grown spontaneous AlGaAs superlattice, Sensor. Actuat. A-Phys. 297, 111548(2019).
6. T. S. Kuan, T. F. Kuech, W. I. Wang and E. L. Wilkie, Long-Range Order in $Al_xGa_{1-x}As$, Phys. Rev. Lett., 54 (1985).
7. A. Gomyo, K. Kobayashi, S. Kawata, I. Hino, T. Suzuki, Studies of $Ga_xIn_{1-x}P$ layers grown by metalorganic vapor phase epitaxy; Effects of V/III ratio and growth temperature, J. Cryst. Growth 77 (1986) 367-373.

8. T. Suzuki, A. Gomyo, S. Iijima, K. Kobayashi, S. Kawata, I. Hino, T. Yuasa, Band-Gap Energy Anomaly and Sublattice Ordering in GaInP and AlGaInP Grown by Metalorganic Vapor Phase Epitaxy, Jpn. J. Appl. Phys. 27 (1988) 11.
9. L.C. Su, S.T. Pu, G.B. Stringfellow, J. Christen, H. Selber, D. Bimberg, Control of ordering in GaInP and effect on bandgap energy, J.Electron. Mater. 23(1994) 125-133.
10. X. Tang, J. Zhao, M.K Chin, T. Mei, Z. Yin, S. Deny, A.Y. Du, Effect of rapid thermal annealing on the ordering of AlInP grown by metal-organic vapor-phase epitaxy, Appl. Phys. Lett 87 (2005).
11. H. R. Jen, M. J. Cherng, G. B. Stringfellow, Ordered structures in $GaAs_{0.5}Sb_{0.5}$ alloys grown by organometallic vapor phase epitaxy, Appl. Phys. Lett. 48 (1986).
12. R. T. Lee, J. K. Shurtleff, C. M. Fetzer, G. B. Stringfellow, S. Lee, T. Y. Seong, Surfactant controlled growth of GaInP by organometallic vapor phase epitaxy, J. Appl. Physics, 87 (2000).
13. M. Kondow, H. Kakibayashi, T. Tanaka, and S. Minagawa, Ordered structure in $Ga_{0.7}In_{0.3}P$ alloy, Phys. Rev. Lett., 63 (1989).
14. M. Ichimura, A. Sassaki, Free Energies and Equilibrium States of Mono- and Bi-Layer Superstructures of III-V Ternary Alloy Semiconductors, Jpn. J. Appl. Phys., 25 (1986) 976-980.
15. G. B. Stringfellow, Calculation of ternary phase diagrams of III–V systems, J. Phys. Chem. Solids, 33 (1972) 665-677.
16. A. Zunger, Spontaneous Atomic Ordering in Semiconductor Alloys: Causes, Carriers, and Consequences, MRS Bull. ,22 (1997) 20-26.
17. W. I. Wang, On the long-range order in AlGaAs, J. Appl. Phys. 58 (1985).
18. M. E. Hoenk, C. W. Nieh, H. Z. Chen, K. J. Vahala, Compositional modulation in $Al_xGa_{1-x}As$ epilayers grown by molecular beam epitaxy on the (111) facets of grooves in a nonplanar substrate, Appl. Phys. Lett. 55 (1989).
19. A. Pradhan, T. Maitra, S. Mukherjee, S. Mukherjee, A. Nayak, B. Satpati, S. Bhunia, Spontaneous superlattice structures in $Al_xGa_{1-x}As$ /GaAs (1 0 0) grown by metalorganic vapor phase epitaxy, Mater. Lett. 210 (2018) 77–79.
20. S. K. Sinha, E. B. Sirota, S. Garoff, H. B. Stanley, X-ray and neutron scattering from rough surfaces, Phys. Rev. B 38 (1988).
21. M. K. Sanyal, S. K. Sinha, A. Gibaud, K. G. Huang, B. L. Carvalho, M. Rafailovich, J. Sokolov, M. X. Zhao, W. Zhao, Fourier reconstruction of density profiles of thin films using anomalous X-ray reflectivity, Europhys. Lett. 21 (1993).

22. M. Sharma, M. K. Sanyal, M. K. Mukhopadhyay, M. K. Bera, B. Saha, P. Chakraborty, Structural and morphological characterization of molecular beam epitaxy grown Si/Ge multilayer using x-ray scattering techniques, J. Appl. Phys. 110 (2011) 102204.
23. S. van Riesen, A. W. Bett, G. P. Willeke, Accelerated ageing tests on III-V solar cells, In: Proceedings of 3rd WCPEC, Osaka; May 11–18 (2003) 837–840.
24. D. A. Vanderwater, I. -H Tan, G. E. Hofler, D. C. Defevere, F. A. Kish, High-brightness AlGaInP light emitting diodes, In: Proceedings of the IEEE, vol. 85,11 (1997) 1752-1764.
25. K. Streubel, N. Linder, R. Wirth and A. Jaeger, High brightness AlGaInP light-emitting diodes, IEEE. J. Sel. Top. Quant., 8 (2002) 321-332.
26. Y. C. Wang, J. M. Kuo, F. Ren, J. R. Lothiani, W. E. Mayo, Schottky barrier heights of $In_{0.5}(Al_xGa_{1-x})_{0.5}P$ ($0 \leq x \leq 1$) lattice matched to GaAs, Solid State Electron, 42 (1998) 1045–1048
27. J. R. Lothian, M. J. Kuo, F. Ren, S. J. Pearton, Plasma and wet chemical etching of $In_{0.5}Ga_{0.5}P$, J. Electron. Mater, 21 (1991) 441.
28. M. O. Watanabe, Y. Ohba, Interface properties for GaAs/InGaAlP heterojunctions by the capacitance- voltage profiling technique, Appl. Phys. Lett., 50 (1987) 906-908.
29. C.-T. Lee, H.-Y. Lee, Metal-semiconductor-metal photodetectors with InAlGaP capping and buffer layers, IEEE Electron Devices Letters 24 (2003) 532.
30. S. Zhao, Z. Mi, AlGaN nanowires: path to electrically injected semiconductor deep ultraviolet lasers, IEEE J. Quantum Electron. 54, 6 (2018).
31. M. Behzadirad, M. Nami, N. Wostbrock, M. R. Zamani Kouhpanji, D. F. Feezell, S. R. Brueck, T. Busani, Scalable top-down approach tailored by interferometric lithography to achieve large-area single-mode GaN nanowire laser arrays on sapphire substrate, ACS Nano 12, 2373 (2018).
32. S. Chu, G. Wang, W. Zhou, Y. Lin, L. Chernyak, J. Zhao, J. Kong, L. Li, J. Ren, J. Liu, Electrically pumped waveguide lasing from ZnO nanowires, Nat. Nanotech. 6, 8 (2011).
33. F. Gao, M. M. Morshed, S. B. Bashar, Y. Zheng, Y. Shi, and J. Liu, Electrically pumped random lasing based on an Au–ZnO nanowire Schottky junction, Nanoscale 7, 9505-9509 (2015).
34. Men, H., Tian, N. & Yu, Electrically pumped random laser from ZnO nanocolumn based on back-to-back Schottky structure, J. Appl. Phys. B 124: 24, (2018).

35. H. Cao, J. Y. Xu, D. Z. Zhang, S. H. Chang, S. T. Ho, E. W. Seelig, X. Liu, R. P. H. Chang, Spatial confinement of laser light in active random media, Phys. Rev. Lett. 84, 5584 (2000).
36. D. M. Bagnall, Y. F. Chen, Z. Zhu, and T. Yao, Room temperature excitonic stimulated emission from zinc oxide epilayers grown by plasma-assisted MBE, Appl. Phys. Lett. 70, 2230 (1997).
37. P. Yu, Z.K. Tang, G.K.L. Wong, M. Kawasaki, A. Ohtomo, H. Koinuma, Y. Segawa, Room-temperature gain spectra and lasing in microcrystalline ZnO thin films, J. Cryst. Growth 184/185, 601 (1998).
38. M. Suja, B. Debnath, S. B. Bashar, L. Su, R. Lake, J. Liu, Electrically driven plasmon-exciton coupled random lasing in ZnO metal-semiconductor-metal devices, Appl. Surf. Sci. 439, 525 (2018).
39. Z. Peterson, R. C. Word, and R. Könenkamp, Structural instability and dynamic emission fluctuations in zinc oxide random lasers, J. Appl. Phys, 124, 063104 (2018).
40. C. Klingshirn, Properties of the electron-hole plasma in II–VI semiconductors, J. Cryst. Growth 117, 753 (1992).
41. W. Wegscheider, L. N. Pfeiffer, M. M. Dignam, A. Pinczuk, K. W. West, S. L. McCall, R. Hull, Lasing from excitons in quantum wires, Phys. Rev. Lett. 71, 4071 (1993).
42. J. A. Alanis, M. Lysevych, T. Burgess, D. Saxena, S. Mokkapati, S. Skalsky, X. Tang, P. Mitchell, A. S. Walton, H. H. Tan, C. Jagadish, P. Parkinson, Large-Scale Statistics for Threshold Optimization of Optically Pumped Nanowire Lasers Nano Lett., Article ASAP (2018).
43. S. Bao, D. Kim, C. Onwukaeme, S. Gupta, K. Saraswat, K. H. Lee, Y. Kim, D. Min, Y. Jung, H. Qiu, H. Wang, E. A. Fitzgerald, C. S. Tan, D. Nam, Low-threshold optically pumped lasing in highly strained germanium nanowires, Nat. Commun. 8, 1845 (2017).
44. M. H. Huang, S. Mao, H. Feick, H. Yan, Y. Wu, H. Kind, E. Weber, R. Russo, P. Yang, Room-temperature ultraviolet nanowire nanolasers, Science, 292, 1897 (2001).
45. A. Vigliante, H. Homma, J. T. Zborowski, T. D. Golding, S. C. Moss, High-resolution x-ray diffraction study of $In_{0.25}Ga_{0.75}Sb$/InAs superlattice, J. Mater. Res. 14 (1999) 1744-1751.
46. J. M. Vandenberg, D. Gershoni, R. A. Hamm, M. B. Panish, H. Temkin, Structural perfection of InGaAs/InP strained- layer superlattices grown by gas source molecular-beam epitaxy: A high- resolution x- ray diffraction study, J. Appl. Phys. 66 (1989).

47. R. L. Forrest, D. W. Stokes, J. H. Li, R. Lukic, T. D. Golding, X-ray diffraction analysis of interdiffusion in $Al_xIn_{1-x}As_ySb_{1-y}$/GaSb multilayers, J. Vac. Sci. Technol., B 24 (2006).
48. Y. Finkelstein, E. Zolotoyabko, M. Blumina, and D. Fekete, Characterization of strained quantum wells by high- resolution x- ray diffraction, J. Appl. Phys. 79 (1996).
49. R. Nouchi, Extraction of the Schottky parameters in metal-semiconductor-metal diodes from a single current-voltage measurement, J. Appl. Phys. 116 (2014) 184505.
50. T. Nishimura, K. Kita, A. Toriumi, Evidence for strong Fermi-level pinning due to metal-induced gap states at metal/germanium interface, Appl. Phys. Lett. 91 (2007) 123123.
51. A.J. Chiquito, C.A. Amorim, O.M. Berengue, L.S. Araujo, E.P. Bernardo, E.R. Leite, Back-to-back Schottky diodes: the generalization of the diode theory in analysis and extraction of electrical parameters of nanodevices, J. Phys. Condens. Matter, 24 (2012) 225303.
52. S. Zhou, M.F. Wu, S.D. Yao, Y.M. Lu, Y.C. Liu, The strain reduction and quality improvement in ZnO film by a 30° in-plane rotation with respect to the Al_2O_3 substrate, Mater. Res. Bull. 41, 2198(2006).
53. Z. L. Wang, Zinc oxide nanostructures: growth, properties and applications, J. Phys. Condens. Matter 16, R829 (2004).
54. Y. P. Varshni, Temperature dependence of the energy gap in semiconductors, Physica 34, 149 (1967).

List of publications related to thesis

1. **T. Maitra**, A. Pradhan, S. Mukherjee, S. Mukherjee, A. Nayak and S. Bhunia. Evaluation of spontaneous superlattice ordering in MOCVD grown $Al_xGa_{1-x}As$ epilayer on GaAs (100) using X-ray reflectivity and rocking curve analysis***, Physica E Low dimensional Systems and Nanostructures,*** 2019, 106, 357-362.

2. **T. Maitra**, A. Pradhan, S. Mukherjee, S. Mukherjee, A. Nayak and S. Bhunia, Temperature and excitation dependent ultraviolet lasing in vertically oriented ZnO nanowires, ***Journal of Materials Science: Materials in Electronics***, (2019) 30: 8814.

3. **T. Maitra**, A. Pradhan, S. Mukherjee, S. Mukherjee, A. Nayak and S. Bhunia, Fast-response Symmetric Coplanar Ni/AlGaInP/Ni Visible Photodetector, ***Sensors and Actuators A: Physical***, 2020, 305, 111933.

List of attended conferences

1. "ISSMD 4 Symposium", Organized by School of materials science and Nanotechnology, Jadavpur University

Venue: Jadavpur University, West Bengal.

Date: 8th-10th March 2017.

Title of the poster presentation and contributors:

Temperature and Excitation Dependent Lasing Characteristics of ZnO Nanorods, **T. Maitra**, A. Pradhan, S. Mukherjee, S. Mukherjee, A. Nayak and S. Bhunia.

2. "3rd International Conference on Condensed Matter and Applied Physics. (ICC-2019)", organized by Govt. Engineering college Bikaner & Ceramic Electrical Research & Development Centre

Venue: Bikaner, Rajasthan.

Date: 14 -15th October 2019.

Title of the poster presentation and contributors:

Probing Interface roughness of the GaAs/$Al_{0.3}Ga_{0.7}As$ Multi-quantum-well Structures Using Low-temperature Photoluminescence Spectra, **T. Maitra**, A. Pradhan, S. Mukherjee, S. Mukherjee, A. Nayak and S. Bhunia.

3. IWPSD 2019, XXth International Workshop on Physics of Semiconductor Devices: IWPSD 2019

Venue: Novotel Hotel and Residences, Kolkata, India

Date: December 17-20, 2019

Title of the poster presentation and contributors:

Visible-NIR photodetector based on Au-Ge/ $(Al_yGa_{1-y})_x In_{1-x} P$ /Ni asymmetric coplanar metal-semiconductor-metal structure, **T. Maitra**, S. Mukherjee, A. Pradhan, S. Mukherjee, A. Nayak and S. Bhunia.